SAND2016-8068J

Molecular Dynamics Analysis of Hydriding / Dehydriding of Palladium Hydrides
Part II: Surface / Interface Thermodynamic and Kinetic Properties

X. W. Zhou[1,*], T. W. Heo[2], B. C. Wood[2], V. Stavila[1], and M. D. Allendorf[1]

[1]*Sandia National Laboratories, Livermore, California 94550, USA*

[2]*Lawrence Livermore National Laboratory, Livermore, California 94550, USA*

ABSTRACT

This work uses molecular dynamics simulations to study surface and interface properties of PdH_x that are relevant to hydrogen storage applications. In particular, surface energies, interfacial energies, surface diffusivities, and surface segregations are all determined as a function of temperature and composition. During the course of the calculations, we demonstrated robust molecular dynamics methods that can result in highly converged finite temperature properties. Challenging examples include accurate calculations of hydrogen surface diffusivities that account for all possible atomic jump mechanisms, and constructions of surface segregation composition profiles that have negligible statistical errors. Our robust calculations reveal that the Arrhenius plots of hydrogen surface diffusion is ideally linear at low compositions, and becomes nonlinear at high compositions. The fundamental cause for this behaviour has been identified. This nonlinear surface diffusion behaviour is also in good agreement with available experimental data for bulk diffusion. The implication of our calculated properties on hydrogen storage application is discussed.

I. INTRODUCTION

[*]Email: xzhou@sandia.gov; Tel.: 925-294-2851

Solid state hydrogen storage materials, in theory, can provide sufficient hydrogen energy for transportation systems that reduce oil dependency and mitigate the long-term effects of fossil fuels on climate change. This has not been realized because progress towards developing commercially viable hydrogen storage materials continues to be hindered by a lack of fundamental understanding of the kinetics and thermodynamics underlying the physical properties of interest. To fill this gap, we have been developing an engineering scale phase field model capable of simulating the kinetics of hydriding and dehydriding processes of interstitial hydrides using PdH_x as an exemplar system[1]. In such an interstitial hydride, hydriding / dehydriding proceeds through changes of relative volume fraction of the hydrogen-poor α and the hydrogen-rich β phases.

Our phase field model implements all major properties believed to impact the hydriding / dehydriding kinetics. These include bulk properties such as lattice constants, Gibbs free energies, elastic constants, and bulk diffusivities, and non-bulk properties such as surface energies, interfacial energies, surface diffusivities, and surface segregation ratios. Here lattice constants and elastic constants (of the α and β phases) are included because they define the lattice mismatch strain energy of an $\alpha + \beta$ microstructure as a function of α and β volume fractions. Surface segregation ratios are considered because they change the composition gradients and hence the diffusion rate of hydrogen between surface and bulk, in addition to their effects on rates of various $H_2 \Leftrightarrow 2H$ chemical processes on the surface. These, along with various other energetic and diffusion properties included in the property list, encompass all the driving forces and kinetics parameters of the phase transformation.

We have also been using molecular dynamics (MD) to calculate the bulk and non-bulk properties listed above. This is because if the input properties of the phase field model are all

calculated from MD simulations, then the hydriding / dehydriding kinetics obtained from the phase field and MD simulations should be identical under the same simulated conditions. MD can therefore guide / validate independently each component in the phase field model. In addition, MD simulations should also reveal correctly the general trends of hydriding / dehydriding kinetics as a function of material structures and operating conditions. Therefore, MD can help interpret experimental observations and establish designing rules for general materials.

In part I of our overall effort[2], we have used MD to calculate all the bulk properties mentioned above. The non-bulk properties, however, have not been determined. One requirement is that all these properties must be determined as a function of temperature and composition in order to be applicable to the entire hydriding / dehydriding processes. This imposes two challenges. First, properties of materials are usually calculated at 0 K using molecular statics (MS) simulations. While time-averaged MD simulations can result in finite temperature properties, the results are not useful unless the statistical errors due to thermal noises are reduced to a negligible level. Second, some properties of our interest here, such as the composition profile (or equivalently, the surface segregation ratio), may involve significant statistical errors if measured only from a snapshot of the final configuration of an MD or MS simulations. Such a composition profile is also extremely sensitive to the initial configuration (in terms of population of different atoms on different lattice sites). Unfortunately, the initial configuration must be randomly created.

Based on the recognitions discussed above, this paper aims to achieve four major objectives: (i) demonstrate time-averaged MD methods capable of calculating highly converged non-bulk properties; (ii) use MD to calculate all relevant non-bulk properties (surface energies, interfacial energies, surface diffusivities, and surface segregation ratios) as a function of both

temperature and composition, and reduce the results to analytical equations for convenience of phase field model developments; and (iii) discuss new physics revealed in the simulations that can help understand the hydrogen storage materials. We point out that this paper is the second part of an overall effort to develop a phase field model for hydrogen storage materials. The first part on MD studies of bulk properties, and the third part on development of the phase field model, are published separately.

II. INTERATOMIC POTENTIAL

Our studies are based on the Pd-H embedded-atom method (EAM) potential we developed[3] previously. This potential particularly suits our purpose because it better captures the experimentally observed phase separation as compared to other literature potentials[4,5,6]. Although the potential overestimates the equilibrium composition of the β phase[2], it should not impact our studies on trends and our goal of guiding the phase field mode development.

III. {111} SURFACE ENERGIES

{111} surface energies are calculated for 10 compositions x = 0.0, 0.1, 0.2, …, 0.9 at four temperatures T = 300, 400, 500, and 600 K, for a total of 40 calculations. The systems contain 3024 palladium atoms on an fcc lattice with 21 {112} planes in the x- direction, 18 {111} planes in the y- direction, and 12{110} planes in the z- direction. Various number of hydrogen atoms are introduced in the octahedral interstitial sites initially to create the target composition. To calculate a finite temperature surface energy, an MD simulation with an NPT ensemble is first performed for 2.3 ns under periodic boundary conditions in all three coordinate directions. After discarding the first 0.1 ns, time-averaged dimensions are calculated for the next 2.2 ns. These time-averaged dimensions are used to create a new crystal that incorporates the thermal expansion effect. Two MD simulations with an NVT ensemble are then used to anneal this new

crystal for 2.3 ns. One simulation uses periodic boundary conditions in all three directions to mimic a bulk crystal. The other simulation uses periodic boundary conditions in the x- and z-directions and a free boundary condition in the y- direction to mimic a crystal with two y-surfaces. After discarding the first 0.1 ns, time-averaged energies are calculated for the next 2.2 ns. The surface energies are calculated as the difference in the time-averaged energies between the NVT crystals with and without the surfaces, scaled to the per surface area unit. Note that we use the NVT ensemble for both bulk and surface calculations. Alternatively, we can use the time-averaged bulk energy obtained from the first MD simulation under the NPT ensemble, but the results will not be as consistent as using NVT for both the bulk and the surface cases.

The calculated MD surface energies γ_s as a function of compositions are fitted to the following polynomial:

$$\gamma_s = \sum_{i=0}^{5}\sum_{j=0}^{2} c_{ij} \cdot x^i \cdot T^j \tag{1}$$

where the fitted coefficient c_{ij} are listed in Table I. The fitted surface energies are compared with MD data in Fig. 1 at two selected temperatures of 300 and 500 K. It can be seen that the fitted curves are in good agreement with the MD data. Fig. 1 also indicates that H dramatically reduces the Pd surface energy, suggesting strong hydrogen-embrittlement effect. On the other hand, PdH_x surface becomes nearly a constant when the composition x is above 0.2. While increasing temperature does not change the surface energy of pure Pd, it does increase the surface energy of PdH_x for $x > 0.4$. This can be understood because different temperatures will cause different H populations near the surface vs. the bulk, as will be shown below.

Table I. {111] surface energy coefficient c_{ij}.

j	i					
	0	1	2	3	4	5
0	0.1316	-0.5935	3.0757	-10.2060	13.2672	-5.6622

1	-0.0000279	-0.0018319	0.0055740	0.0059203	-0.0213158	0.0117988
2	0.0311×10^{-6}	1.7641×10^{-6}	-5.2651×10^{-6}	-5.8792×10^{-6}	20.6013×10^{-6}	-11.3648×10^{-6}

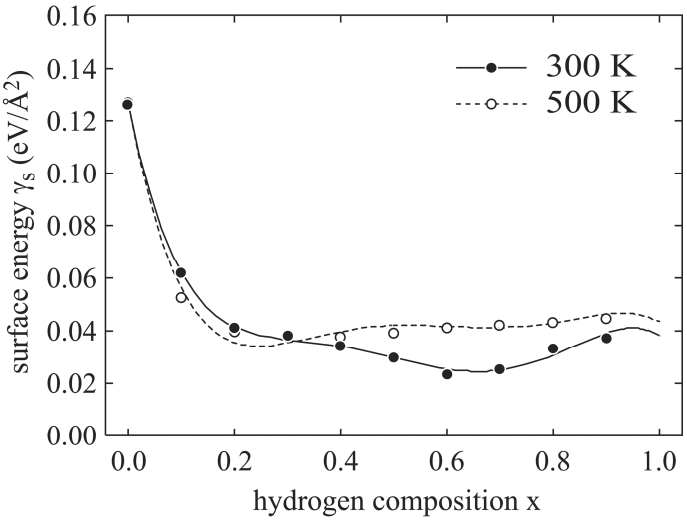

Fig. 1. {111} surface energy as a function of composition at two selected temperatures of 300 and 500 K.

IV. INTERFACIAL ENERGIES

Energy between a coherently bonded α/β interface is sensitive to local strain energy, and therefore depends on volume fraction f_β, temperature T, interfacial thickness w, and α and β compositions x_α and x_β. Unlike the other properties, we could not find a highly converged MD method to calculate interfacial energy accounting for all these variables. Instead, we can derive an interfacial energy expression in terms of other properties. First, origin of interfacial energy is explored. In Figs. 2(a) and 2(b), we illustrate the composition profiles of a sharp and a diffused interface respectively. For simplicity, we assume that the composition of the diffused interface linearly changes over the width w. The local energy density is composed of chemical (e.g., heat of formation) and strain energy contributions. Under the assumption that both chemical and strain energies are functions of composition only, the composition profiles shown in Figs. 2(a) and 2(b) would mean that the local energy density is a step function for the sharp interface and a

smooth function for the diffused interface as depicted in Fig. 2(c). For the sharp interface, the step function means that the total energy is simply sum of the energies of independent α and β phases, and as a result, no interfacial energy exists. This is indeed true for an ideally sharp continuum interface where no region would have a composition different from those of the two phases. Atomistic systems always have interfacial energies even the two phases both have uniform compositions. This, however, is consistent with the continuum picture because atomistic systems can never have truly sharp interfaces because atoms at an interface always have different local compositions (i.e., they interact with atoms in the other phase) from atoms far away from the interface. In other words, the sharpest atomistic interface is diffused in continuum concept by at least one atomic plane spacing. Based on these recognitions, Fig. 2(d) shows the energy difference between the diffused and sharp interfaces. The interfacial energy can then be calculated as the total integral of this energy difference, scaled to a per interfacial area unit.

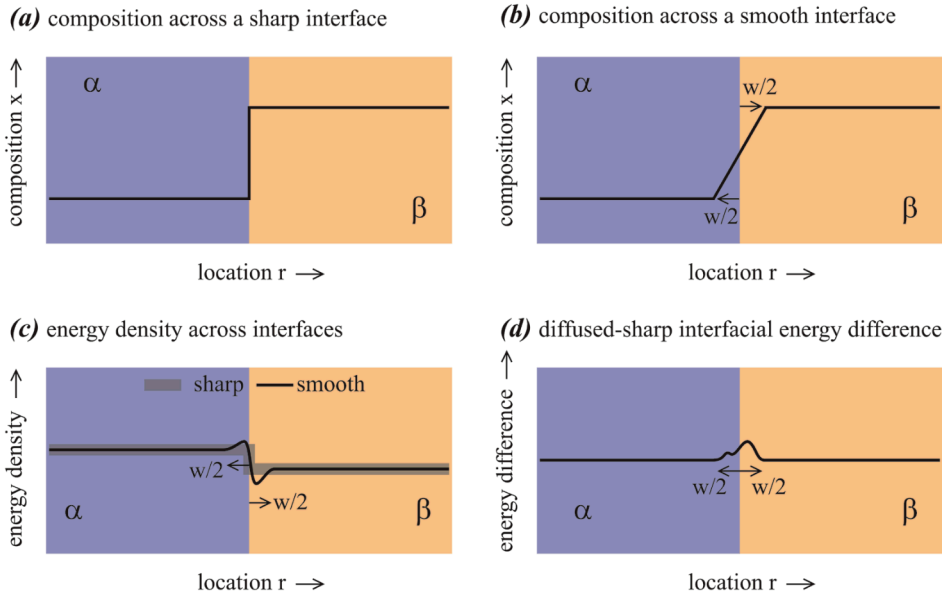

Fig. 8. Illustration of origin of interfacial energy between α and β phases: (a) composition profile across a sharp interface; (b) composition profile across a diffused interface with a width of w; (c) sum of strain and chemical energy densities across sharp (thick light line) and diffused (thin dark line) interfaces; and (d) interfacial energy taken as the total energy difference between the diffused and sharp interfaces, scaled to per interfacial area unit.

To derive an interfacial energy expression, we assume that the volume fraction of the β phases is f_β. The volume fraction of the α phase is then 1- f_β. The lattice constants of free α and β phases can be written in terms of functions of composition and temperature as $a_\alpha = a(x_\alpha,T)$, and $a_\beta = a(x_\beta,T)$ respectively, where x_α and x_β are the compositions of the α and β phases. The unit cell volume of the free α and β phases are $V_\alpha = [a(x_\alpha,T)]^3$, and $V_\beta = [a(x_\beta,T)]^3$. When the α and β are equilibrated in a microstructure, the lattice constants or the unit cell volumes of the α and β phases are equal. Hence, we can write:

$$V = V_\alpha \cdot \left(1+\varepsilon_{V,\alpha}\right) = V_\beta \cdot \left(1+\varepsilon_{V,\beta}\right) \tag{2}$$

where $\varepsilon_{V,\alpha}$ and $\varepsilon_{V,\beta}$ are volumetric strain of the α and β phases, and V is the overall unit cell volume of the system. On the other hand, the overall stress of the system vanishes, and therefore we have

$$\left(1-f_\beta\right)\cdot B\left(x_\alpha,T\right)\cdot\varepsilon_{V,\alpha} + f_\beta \cdot B\left(x_\beta,T\right)\cdot\varepsilon_{V,\beta} = 0 \tag{3}$$

where B(x,T) is bulk modulus as a function of composition and temperature. From Eqs. (2) and (3), we can derive:

$$\varepsilon_{V,\alpha} = \frac{1}{1+\dfrac{1-f_\beta}{f_\beta}\cdot\dfrac{V_\beta}{V_\alpha}\cdot\dfrac{B\left(x_\alpha,T\right)}{B\left(x_\beta,T\right)}}\frac{V_\beta - V_\alpha}{V_\alpha} \tag{4}$$

Similarly, we can also derive:

$$\varepsilon_{V,\beta} = \frac{1}{1+\dfrac{f_\beta}{1-f_\beta}\cdot\dfrac{V_\alpha}{V_\beta}\cdot\dfrac{B\left(x_\beta,T\right)}{B\left(x_\alpha,T\right)}}\frac{V_\alpha - V_\beta}{V_\beta} \tag{5}$$

Both Eqs. (4) and (5) can be used to derive the interfacial energy. For clarity, we use Eq. (4).

In Eq. (4), $(V_\beta-V_\alpha)/V_\alpha$ is the volumetric mismatch of the α phase with respect to the β phase, i.e., the strain required for the α phase to match exactly the unstrained β phase. In our case, V_α and V_β are close. It can then be seen that $\varepsilon_{V,\alpha}$ approaches $(V_\beta-V_\alpha)/V_\alpha$ when the majority of the system is the β phase, i.e., $(1-f_\beta)/f_\beta \approx 0$, or the β phase is much stiffer than the α phase, i.e., $B(x_\alpha,T)/B(x_\beta,T) \approx 0$. These are all consistent with physical intuition.

Substituting Eq. (4) into Eq. (2), the unit cell volume V can be derived as

$$V = \frac{\left(1-f_\beta\right)\cdot B\left(x_\alpha,T\right)+f_\beta\cdot B\left(x_\beta,T\right)}{\left(1-f_\beta\right)\cdot V_\beta\cdot B\left(x_\alpha,T\right)+f_\beta\cdot V_\alpha\cdot B\left(x_\beta,T\right)}\cdot V_\alpha\cdot V_\beta \tag{6}$$

The volumetric strain for any interfacial region with a composition x in an elastically equilibrated α + β microstructure can be expressed as

$$\varepsilon_V\left(x,T,f_\beta,x_\alpha,x_\beta\right)=\frac{V-\left[a(x,T)\right]^3}{\left[a(x,T)\right]^3} \tag{7}$$

Here a(x,T) is lattice constant as a function of composition and temperature. Note that Eq. (7) specifically indicates that ε_V is a function of x, T, f_β, x_α, and x_β. The elastic energy per atom of any region with composition x is then

$$E_e\left(x,T,f_\beta,x_\alpha,x_\beta\right)=\frac{1}{2}B\left(x,T\right)\cdot\varepsilon_V^2\left(x,T,f_\beta,x_\alpha,x_\beta\right)\cdot\Omega\left(T,f_\beta,x_\alpha,x_\beta\right) \tag{8}$$

where $\Omega(x,T) = [a(x,T)]^3/[4(1+x)]$ is atomic volume. According to the discussions above, the interfacial energy γ_i can then be calculated as

$$\gamma_i\left(f_\beta,T,w,x_\alpha,x_\beta\right)= \int_{-w/2}^{w/2}\frac{\Delta H_f\left(x,T\right)+E_e\left(x,T,f_\beta,x_\alpha,x_\beta\right)}{\Omega\left(x,T\right)}dr- \left[\frac{\Delta H_f\left(x_\alpha,T\right)+E_e\left(x_\alpha,T,f_\beta,x_\alpha,x_\beta\right)}{\Omega\left(x_\alpha,T\right)}+\frac{\Delta H_f\left(x_\beta,T\right)+E_e\left(x_\alpha,T,f_\beta,x_\alpha,x_\beta\right)}{\Omega\left(x_\beta,T\right)}\right]\frac{w}{2} \tag{9}$$

where $\Delta H_f(x,T)$ is heat of formation as a function of composition and temperature, and the composition x is expressed as a linear function of position r as $x = x_\alpha + (x_\beta - x_\alpha)\cdot(r + w/2)/w$ as stated above. Explicit expressions for lattice constant a(x,T), bulk modulus B(x,T), and heat of formation $\Delta H_f(x,T)$ are all given previously[2]. Eqs. (6)-(9) can then be used to calculate the interfacial energy.

Using T = 300 K, $x_\alpha = 0.1$ and $x_\beta = 0.9$ (estimated from the previous work[2]), and w = 15 Å as typically seen in MD simulations, the interfacial energy is calculated as a function of f_β, and the results are shown in Fig. 3. For comparison, the chemical and strain energy contributions are also separately included.

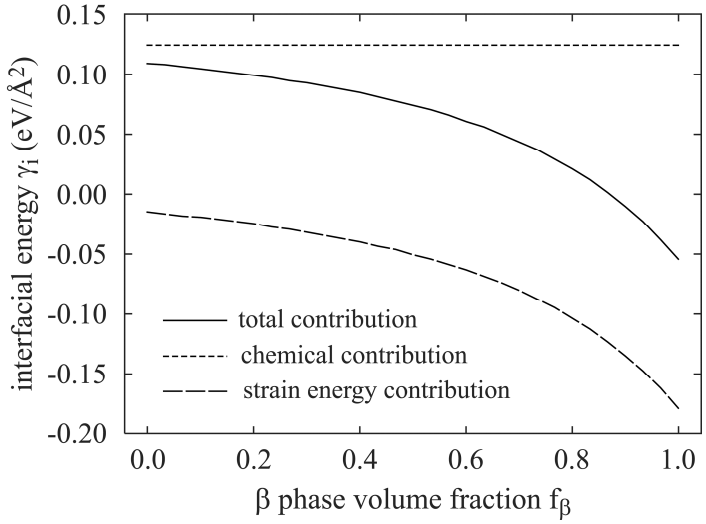

Fig. 3. Interfacial energy as a function of β volume fraction at T = 300 K, $x_\alpha = 0.1$, $x_\beta = 0.9$, and w = 15 Å.

Fig. 3 shows that as hydriding proceeds (f_β increase), the interfacial energy monotonically decreases, and can eventually become negative when f_β approaches 1. Furthermore, chemical contribution is constant and positive with respect to f_β, and it is the strain energy that causes this decrease. This makes sense because the heat of formation favours the sharp interface (i.e., phase separation to compositions x_α and x_β), and as a result, the formation of a smooth composition

variation causes an extra energy. The smooth composition variation, however, would release the misfit strain energy at the interfacial region, and hence can cause the interfacial energy to decrease or even become negative values. When f_β approaches 1, the strain of the α phase reaches the maximum value of $(V_\beta - V_\alpha)/V_\alpha$ according to Eq. (4). This leads to a large strain energy due to the large bulk modulus of the α phase as seen in the previous work[2]. This strain energy, however, pertains to the bulk α and does not belong to the interface. Because a large portion of a high bulk strain energy is released by the interface, the strain energy contribution of the interface becomes the most negative when f_β approaches 1.

V. SURFACE DISSUSIVITIES

Diffusion is usually studied through calculations of diffusion energy barriers for each atomic jump path using molecular statics simulations in combination of a nudged elastic band method[7,8,9]. The problem is that practical materials often involve thousands of atomic jump paths not know a priori. It is also unclear as how to relate thousands of atomic jump events to an overall diffusion behaviour seen in experiments. An often more effective approach is to calculate diffusivities directly from the mean square displacement of diffusion species seen in MD simulations. Diffusivities at different temperatures can then be fitted to Arrhenius equation to get an overall diffusion energy barrier and an overall pre-exponential factor. Despite the many advantages, such an MD-based Arrhenius approach was not widely used due to its significant statistical errors. However, we recently found that when the simulation time is sufficiently long, the statistical errors can be reduced to a negligible level[2,10]. Here we extend this method to the hydrogen surface diffusion problem.

A. Calculations

Surface diffusion on the {111} plane is considered. The crystal used for the system is shown in Fig. 4. It contains 1008 palladium atoms on an fcc lattice with 21 {112} planes in the x- direction, 6 {111} planes in the y- direction, and 12{110} planes in the z- direction. By using periodic boundary conditions in the x- and z- direction and a free boundary condition in the y- direction, this crystal has two {111} surfaces in the y- direction. Various numbers of hydrogen atoms are introduced into the octahedral sites on the top and bottom surface layers. Hence, the systems we study have various H compositions on the two surfaces but the bulk is still pure Pd. 14 PdH_x compositions x = 0.0059, 0.05, 0.10, 0.15, 0.20, 0.25, 0.30, 0.35, 0.40, 0.50, 0.60, 0.70, 0.80, 0.90 are studied. Note that for the system size used here, x = 0.0059 corresponds to a single hydrogen atom on each of the top and bottom surfaces.

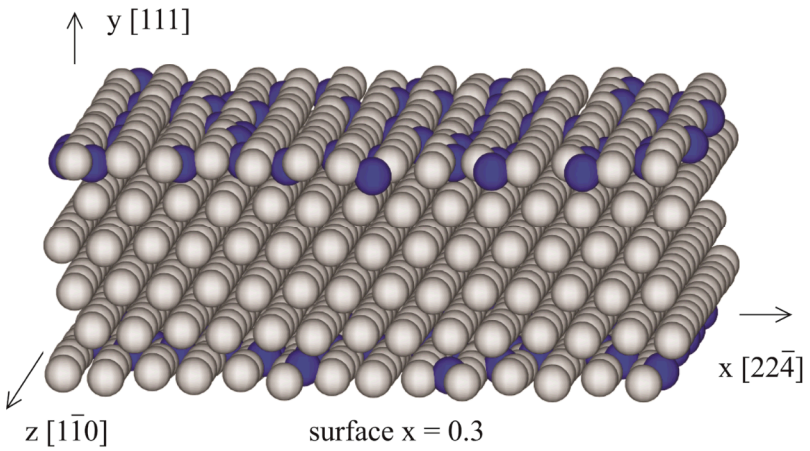

Fig. 4. An example configuration used for surface diffusion simulations.

Using an NPT ensemble, 182 MD simulations are performed to a matrix of the 14 samples and 13 temperatures T = 300, 325, 350, …, 600 K, for a total period of 3.45 ns. After the first 0.15 ns is discarded, the hydrogen positions are output every Δt = 3.3 ps for the remaining 3.3 ns simulation. These hydrogen positions are used to calculate the mean square displacement (only on the surface plane) as a function of time. We notice that majority of hydrogen atoms diffuse on

the surface plane. The hydrogen atoms that diffuse into the bulk are excluded from the mean square displacement calculations. The time derivative of the mean square displacement δ is used to calculate diffusivities D according to D = δ/4 (note D = δ/6 for 3D bulk diffusion). The diffusivities at different temperatures are used to construct the Arrhenius plots. Example Arrhenius plots are shown in Figs. 5(a)-5(d) for four representative compositions: x = 0.1, 0.2, 0.6, and 0.8. It can be seen from Fig. 5 that like bulk diffusion[2], the Arrhenius plots are linear low compositions, and become non-linear at high compositions.

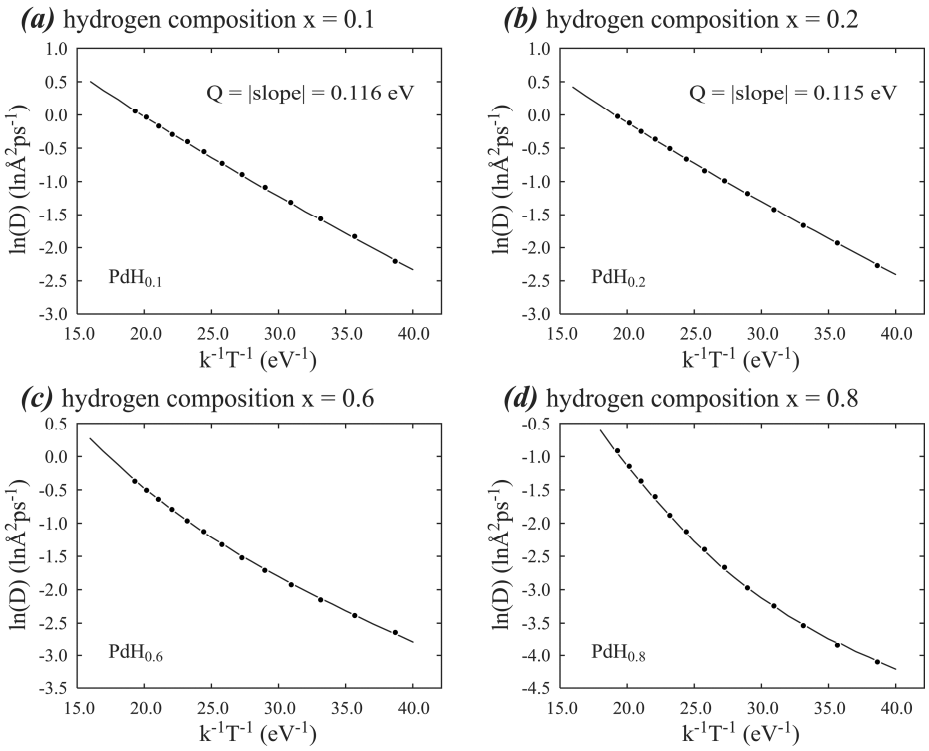

Fig. 5. Arrhenius plots of hydrogen surface diffusion at different hydrogen compositions of (a) x = 0.1; (b) x = 0.2; (c) x = 0.6; and (d) x = 0.8.

B. Two-Mechanism Model

It has been established that the non-linear behaviour seen in Figs. 5(c) and 5(d) can be well described by a two-mechanism model[2]. Based on this model, the hydrogen surface diffusivity is expressed as

$$D = D_{0,1} \cdot \exp\left(-\frac{Q_{0,1}}{kT}\right) + D_{0,2} \cdot \exp\left(-\frac{Q_{0,2}}{kT}\right) \quad (10)$$

where $D_{0,1}$ and $Q_{0,1}$ are pre-exponential factor and diffusion energy barrier for the first diffusion mechanism, and $D_{0,2}$ and $Q_{0,2}$ are the same parameters for the second diffusion mechanism. Fitting Eq. (10) to all the MD data (at x = 0.0059, 0.05, 0.10, 0.15, 0.20, 0.25, 0.30, 0.35, 0.40, 0.50, 0.60, 0.70, 0.80, 0.90) leads to the following parameters:

$$Q_{0,1} = 0.10258 + 0.05758 \cdot x - 0.23045 \cdot x^2 + 0.15401 \cdot x^3 \quad (11)$$

$$D_{0,1} = 6.54187 + 4.36164 \cdot x - 34.01210 \cdot x^2 + 23.56700 \cdot x^3 \quad (12)$$

$$Q_{0,2} = 0.19956 + 0.27303 \cdot x - 0.50115 \cdot x^2 + 0.40175 \cdot x^3 \quad (13)$$

$$D_{0,2} = 17.95170 - 43.19180 \cdot x + 175.62400 \cdot x^2 + 25.65670 \cdot x^3 \quad (14)$$

where $D_{0,1}$ and $D_{0,2}$ are in unit $Å^2$/ps, and $Q_{0,1}$ and $Q_{0,2}$ are in unit eV. The solid lines shown in Figs. 5(a)-5(d) are calculated from Eqs. (10)-(14). It can be seen that the fitted curves match the MD data extremely well, further confirming the two-mechanism model on surface diffusion.

Diffusion energy barriers and pre-exponential factors calculated using Eqs. (11)-(14) are examined in Figs. 6(a) and 6(b) respectively. It can be seen from Fig. 6(a) that the low diffusion energy barrier is nearly a constant, and the high barrier approximately varies between 0.20 and 0.40 eV. Furthermore, Fig. 6(b) indicates that the pre-exponential factor for the low barrier mechanism decays to zero as composition is increased, albeit slowly. On the other hand, the pre-exponential factor for the high barrier mechanism increases with composition. These observations are all similar to the bulk diffusion. As will be shown below, the low barrier is associated with the diffusion of a single hydrogen atom, and the high barrier is associated with the diffusion of a hydrogen atom with rich hydrogen neighbours. Hence, the pre-exponential

factor for the lower barrier event should be highest at low compositions, and the pre-exponential factor for the higher barrier event should be highest at high compositions, in good agreement with Fig. 6.

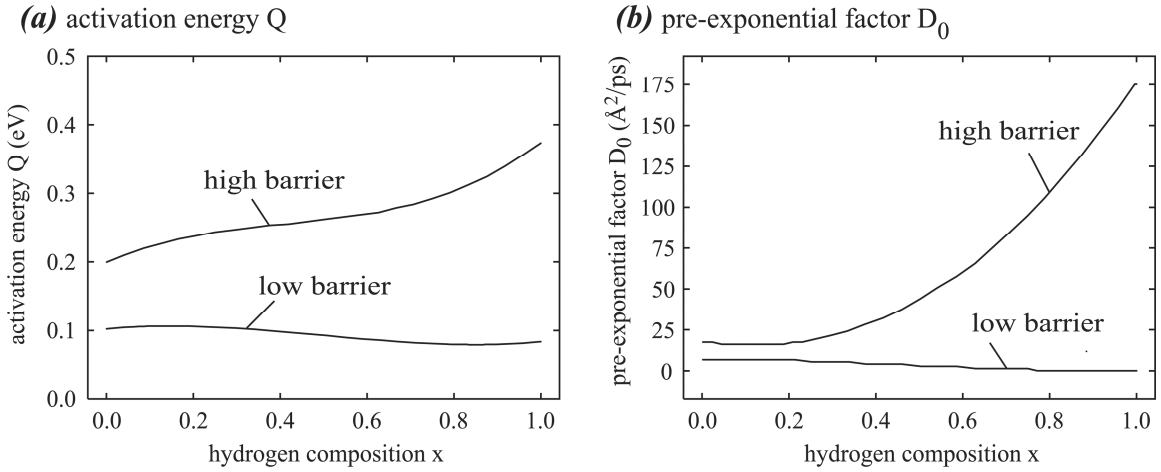

Fig. 6. (a) diffusion energy barriers and (b) pre-exponential factors as a function of composition.

1. MS Corroboration of Mechanisms

A variety of different surface atomic jump paths are present when the system contains many surface hydrogen atoms because these hydrogen atoms can dynamically form different local configurations. In order to corroborate the two-mechanism model, however, we only need to identify a low composition jump path that has a lower energy barrier, and a high composition jump path that has a higher barrier. Two samples with a low composition (one single surface hydrogen atom) and a high composition (a hydrogen surface occupancy fraction x = 0.6) are explored. The computational cells contain 15 {112} planes in the x- direction, 6 {111} planes in the y- direction, and 9 {110} planes in the z- direction. Small portions of the samples near the jumping hydrogen atoms are shown respectively in Fig. 7 (a) and 7(b).

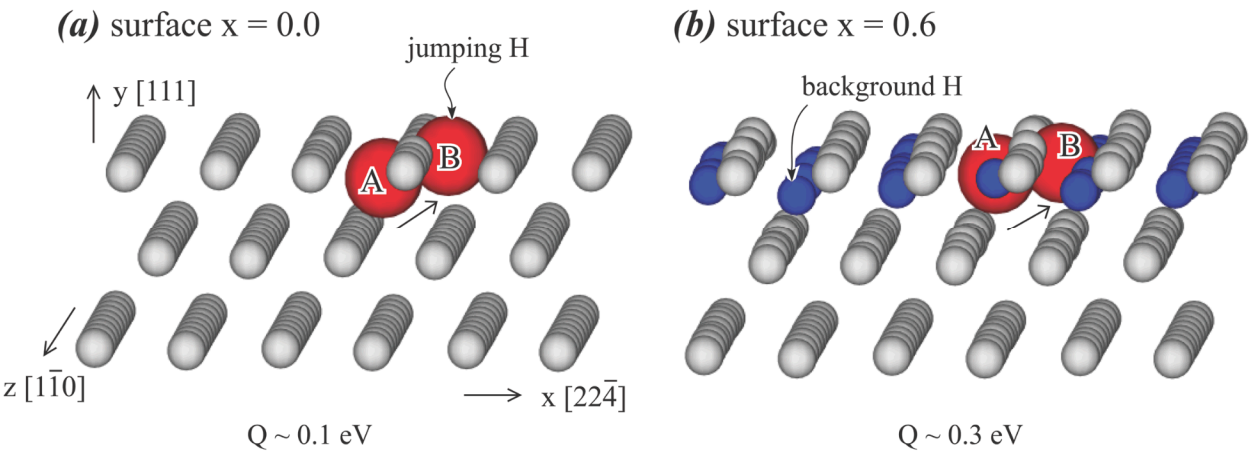

Fig. 7. Diffusion mechanisms at (a) a low and (b) a high composition.

Using the nudged elastic band method[7,8,9], molecular statics simulations are performed to calculate the energy barrier for the jumping hydrogen atoms (big red balls in Fig. 7) to jump from an initial octahedral site (marked as "A") to a neighbouring tetrahedral site (marked as "B"). We find that the low composition jump path, Fig. 7(a), has an energy barrier of about 0.1 eV. The high composition jump path, Fig. 7(b), has a higher energy barrier of about 0.3 eV. More remarkably, these low and high energy barriers are close to the apparent low and high energy barriers obtained from MD simulations as shown in Fig. 6(a). These results strongly validate the two-mechanism model and elucidate the fundamental cause for the nonlinear Arrhenius plots seen in Figs. 5(c) and 5(d).

VI. {111} SURFACE SEGREGATION

The crystals used for the {111} surface segregation studies contain 5040 Pd atoms with 21 {112} in the x- direction, 20 {111} planes in the y- direction, and 12 {110} planes in the z-direction. Based on an NPT ensemble to relax stresses, 60 MD simulations are performed for 6 temperatures T= 100, 200, …, 600 K and 10 compositions x = 0.1, 0.2, …, 1.0. Corresponding number of H atoms are introduced into the octahedral interstitial sites to create the target H

composition. Due to the surface segregation and the finite system size, however, the equilibrium bulk composition x_{bulk} differs from the input composition x. As a result, our analysis uses the bulk composition as the reference.

To simulate the {111} surfaces in the y- direction, periodic boundary conditions are used in the x- and z- directions and a free boundary condition is used in the y- direction. To ensure a full equilibration between the surfaces and bulk, we first perform a pre-conditioning MD simulation that involves 1.5 ns annealing at 600 K, another 1.5 ns to cool the system from 600 K to the target temperature T, and a final 1.5 ns annealing at the target temperature. With the pre-conditioned sample, a second MD simulation is performed for 33 ns at the target temperature, where 100 snapshots of atom positions are recorded on a time interval of 330 ps. Hydrogen composition is calculated for each atomic layer and is averaged over the 100 snapshots. Using the case of T = 300 K and $x_{bulk} = 0.03$ (corresponds to the input composition x = 0.1) as a representative example, the atomic configuration and composition profile normal to the surface are shown respectively in Figs. 8(a) and 8(b).

Figs. 8(a) shows visually a strong H surface segregation effect. This is confirmed in Fig. 8(b) where the surface composition reaches the saturation value of 1.0 as compared to the bulk value of $x_{bulk} \sim 0.03$. Also it is important to note that the composition profile is highly symmetric with respect to the two end surfaces and the composition is ideally constant in the bulk region. This strongly indicates that our high temperature pre-annealing and the average over 100 snapshots have created highly equilibrated hydrogen population and highly converged composition profile. This is an important finding. For example, a highly converged composition profile would not have been achieved if it had not been averaged over 100 snapshots.

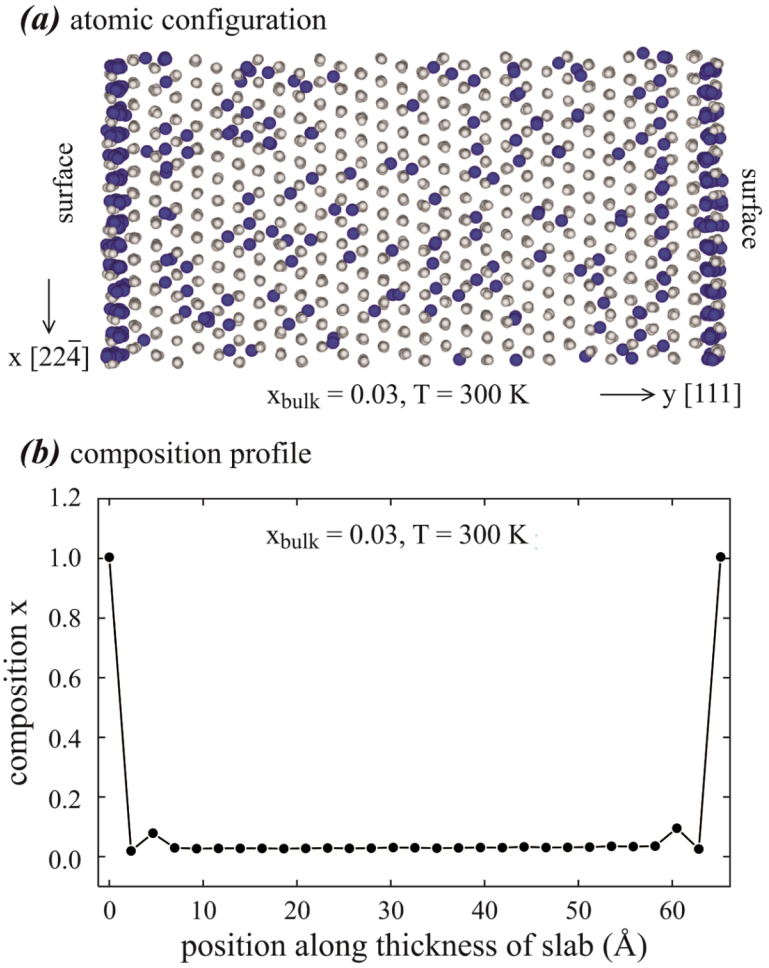

Fig. 8. Surface segregation observation from (a) atomic configuration and (b) composition profile.

The extent of surface segregation can be fully characterized by the surface to bulk composition ratio x_{surf}/x_{bulk}. This parameter is calculated for all MD simulations and the results for two representative temperatures of 100 and 600 K are shown as the data points in Fig. 9. Based on the trends revealed in Fig. 9, the MD data is fitted to the following equation:

$$x_{surf} / x_{bulk} = \frac{2.07555 + 39.62862\exp\left(-5.90611 x_{bulk}\right)}{1 + 0.00829\exp\left(0.00564T\right)} \tag{15}$$

The results calculated using Eq. (15) are included in Fig. 9 as the curves. It can be seen that the fitted curves capture the MD data extremely well.

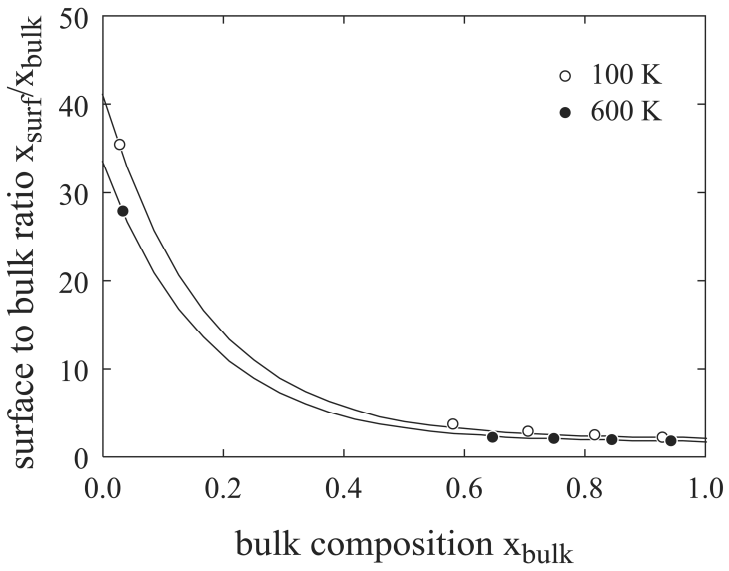

Fig. 9. Surface to bulk composition ratio x_{surf}/x_{bulk} as a function of bulk composition x_{bulk} at two selected temperatures of 100 and 600 K.

Fig. 9 shows that the surface to bulk composition ratio monotonically reduces as the bulk composition increases towards to saturated value of one, consistent with the notion that surface composition is also limited by the saturated value. Temperature is seen to slightly reduce the x_{surf}/x_{bulk}, consistent with the notion that entropy promotes uniform composition. Fig. 9 also indicates the surface concentration can be more than one order of magnitude higher than the bulk concentration when the bulk concentration is low (i.e., at the initial stage of hydriding). This finding is important for nanostructured hydrogen storage materials with high surface area to volume ratio. In particular, a high x_{surf}/x_{bulk} ratio suggests that it is possible to have a separate hydrogen desorption peak due to the surface hydrogen atoms, which is in fact observed in some nanostructured hydrogen storage materials. Finally, Fig. 9 indicates that when the hydrogen is fully charged so that x_{bulk} approaches the saturated value of unity, the x_{surf}/x_{bulk} ratio appears to be around two. This is because the saturated PdH corresponds to hydrogen occupying all the octahedral interstitial sites. However, hydrogen can still occupy tetrahedral interstitial sites.

Furthermore, our composition is calculated by counting the number of hydrogen atoms in each {111} layer. It can be seen from Fig. 8(a) that on the two {111} surfaces, hydrogen not only occupies the octahedral sites just below the Pd surface layers, but can also occupy additional interstitial sites above the surfaces when sub-surface sites are fully occupied.

VII. SUMMARY

Time-averaged MD simulations have been used to generate high quality finite temperature non-bulk properties of PdH_x that are relevant to hydriding and dehydriding processes. The following achievements are useful in future research on both hydrogen storage materials, and atomistic calculations of finite temperature properties:

1. We have demonstrated and validated robust MD methods to calculate highly converged Arrhenius equations for surface diffusion regardless system complexity, number of atomic jumps, and system composition;
2. We have confidently predicted that the Arrhenius plots of hydrogen surface diffusion in PdH_x are perfectly linear at low compositions, but nonlinear at high compositions. This is in good agreement with previous experiments and simulations in bulk PdH_x. We found that the nonlinear can be explained by a two-mechanism model. At low compositions, diffusion occurs through hops of a hydrogen atom with similar environments, and hence a single apparent diffusion energy barrier. At high compositions, diffusion occurs through hops of hydrogen atoms with a range of different environments, and is therefore associated with at least two energy barriers. The smooth variation of relative weight of different hops with respect to temperature then gives a non-linear Arrhenius curve;

3. We have demonstrated that MD methods can produce highly converged composition profiles and surface segregation ratio. A high surface to bulk composition ratio is discovered at low bulk compositions, which explains the separate early desorption peak seen in experiments.

4. We have fitted MD data on surface energies, surface diffusivities, and surface segregation ratios to analytical equations as functions of temperature and composition. We have also derived analytical expression for interfacial energies as functions of relative volume fractions of phases, temperature, interfacial width, and α and β equilibrium compositions. We have demonstrated that these analytical equations capture MD data extremely well. This greatly facilitate future research on PdH_x including phase field modelling of hydriding / dehydriding processes.

VIII. ACKNOWLEDGEMENTS

Sandia National Laboratories is a multiprogram laboratory managed and operated by Sandia Corporation, a wholly owned subsidiary of Lockheed Martin Corporation, for the US Department of Energy's National Nuclear Security Administration under contract DE-AC04-94AL85000. The authors gratefully acknowledge research support from the U.S. Department of Energy, Office of Energy Efficiency and Renewable Energy, Fuel Cell Technologies Office, under Contract Number DE-AC04-94AL85000.

References

1 Tae Wook to provide reference.
2 Zhou, X. W.; Heo, T. W.; Wood, B. C.; Stavila, V.; Allendorf, M. D. Molecular Dynamics Analysis of Hydriding / Dehydriding of Palladium Hydrides. Part I: Bulk Thermodynamic and Kinetic Properties. Submitted.
3 Zhou, X. W.; Zimmerman, J. A. An Embedded-Atom Method Interatomic Potential for Pd-H Alloys. *J. Mater. Res.* **2008**, 23, 704-718.
4 Ruda, M.; Crespo, E. A.; Ramos de Debiaggi, S. Atomistic Modeling of H Absorption in Pd Nanoparticles. J. Alloys Comp. **2010**, 495, 471-475.

5 Ramos de Debiaggi, S.; Crespo, E. A.; Braschi, F. U.; Bringa, E. M.; Ali, M. L.; Ruda, M. Hydrogen Absorption in Pd Thin-Films. Inter. J. Hydro. Ener. **2014**, 39, 8590-8595.
6 Kowalczyk, P; Terzyk, A. P.; Gauden, P. A.; Furmaniak, S.; Kaneko, K. Toward in silico Modeling of Palladium–Hydrogen–Carbon Nanohorn Nanocomposites. Phys. Chem. Chem. Phys. **2014**, 16, 11763-11769.
7 Henkelman, G; Jonsson, H. Improved Tangent Estimate in the Nudged Elastic Band Method for Finding Minimum Energy Paths and Saddle Points. J. Chem. Phys. **2000**, 113, 9978-9985.
8 Henkelman, G; Uberuaga, B. P; Jonsson, H. A Climbing Image Nudged Elastic Band Method for Finding Saddle Points and Minimum Energy Paths. J. Chem. Phys. **2000**, 113, 9901-9904.
9 Nakano, A. A Space-Time-Ensemble Parallel Nudged Elastic Band Algorithm for Molecular Kinetics Simulation. Comp. Phys. Comm. 2008, 178, 280-289.
10 Zhou, X. W.; Gabaly, F. El.; Stavila, V.; Allendorf, M. D. Molecular Dynamics Simulations of Hydrogen Diffusion in Aluminum. J. Phys. Chem. C. **2016**, 120, 7500-7509.